HHS Public Access

Author manuscript

Mater Sci Eng C Mater Biol Appl. Author manuscript; available in PMC 2018 July 01.

Published in final edited form as:

Mater Sci Eng C Mater Biol Appl. 2017 July 01; 76: 301–312. doi:10.1016/j.msec.2017.02.167.

Zn-3Li Alloy after Extrusion and Drawing: Structural, Mechanical Characterization, and Biodegradation in Abdominal Aorta of Rat

Shan Zhao[1], **Jan-M. Seitz**[1], **Rainer Eifler**[3], **Hans J. Maier**[3], **Roger Guillory**[2], **Elisha Earley**[2], **Adam Drelich**[1], **Jeremy Goldman**[2], and **Jaroslaw W. Drelich**[1,*]

[1]Department of Materials Science and Engineering, Michigan Technological University, Houghton, Michigan, USA

[2]Department of Biomedical Engineering, Michigan Technological University, Houghton, Michigan, USA

[3]Institut für Werkstoffkunde (Materials Science), Leibniz Universität Hannover, Garbsen, Germany

Abstract

Zinc shows great promise as a bioabsorbable metal. Our early in vivo investigations implanting pure zinc wires into the abdominal aorta of Sprague-Dawley rats revealed that metallic zinc does not promote restenotic responses and may suppress the activities of inflammatory and smooth muscle cells. However, the low tensile strength of zinc remains a major concern.

A cast billet of the Zn-Li alloy was produced in a vacuum induction caster under argon atmosphere, followed by a wire drawing process. Two phases of the binary alloy identified by x-ray diffraction include the zinc phase and intermetallic $LiZn_4$ phase. Mechanical testing proved that incorporating 3 at.% of Li into Zn increased its ultimate tensile strength from 116 ± 13 MPa (pure Zn) to 274 ± 61 MPa while the ductility was held at 17 ± 7%. Implantation of 10 mm Zn-3Li wire segments into abdominal aorta of rats revealed an excellent biocompatibility of this material in the arterial environment. The biodegradation rate for Zn-3Li was found to be about 0.008 mm/yr and 0.045 mm/yr at 2 and 12 months, respectively.

Graphical abstract

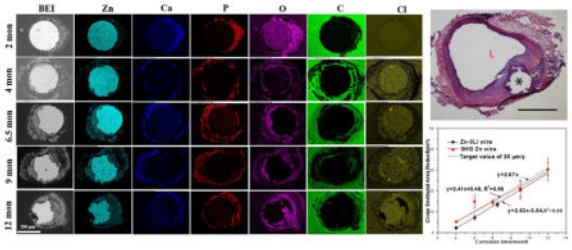

*Corresponding author: jwdrelic@mtu.edu (Jaroslaw W. Drelich).

1. Introduction

Followed by decades of developing strategies to minimize the corrosion of metallic biomaterials, there is now an increasing trend to use absorbable metals in medical applications [1]. The concept of absorbable metals stents (AMS) was envisaged to treat the disease of artery occlusions and then disappear harmlessly when they are no longer needed as mechanical scaffolding. Since the major effect of stent implantation is provided by its scaffolding, it is required to be retained for 6–12 months during which time arterial remodeling and healing is completed [2]. After this period, the stent is preferred to be broken down and excreted by the body, leaving behind a natural functioning artery. The advances of AMS for vascular scaffolding may allow for circumventing the long term risks of permanent stents, such as chronic inflammation, late stage thrombosis (clotting) and stent strut disruption (fracture) [3]. In pediatric intervention, which involves arteries that have not completed their growth cycle, the disappearance of the stent would enable natural vessel growth and avoid the need for recatheterization and serial stent balloon dilatation until adulthood [4]. Thus, the development of biodegradable stents, which can fulfill the mission and step away, is the next logical progression for the industry [5–7].

Mg-based and Fe-based materials have been widely investigated as potential base materials in recent years due to their biocompatible elements and mechanical characteristics [2, 8–10]. However, previous corrosion studies with bare Mg- and Fe-based metals demonstrated that their *in vivo* degradation performance cannot satisfy the requirement for the coronary stent yet. Tremendous work on improvement has been focused on: (1) pure Mg and pure Fe and their alloying with essential elements (Ca, Sr, Zn, Co, C and Si) or low contents of toxic elements (Mn, Sn and Zr), and the rare earth elements (Y and Gd) [11–17]; (2) novel structured biodegradable metals (porous, ultrafine, nanocrystalline and glassy structures) [18–20]; (3) surface modifications by mechanical, chemical and electrochemical treatment [21, 22]. Presently, with the exception of the limus-eluting bioresorbable magnesium scaffold introduced in 2016 by Biotronic, these modifications have not resulted in a biodegradable metallic stent with clinical success.

With the purpose of searching for suitable alloying elements, zinc as one of the most abundant nutritionally essential elements in the human body [23] began to be studied as an alloying element or bioresorbable base material [24]. In 2011, Vojtech et al. [25] prepared binary Zn-Mg alloys containing Mg content up to 3 wt.%, and found that the binary Zn-Mg alloys exhibited corrosion rates (≈0.018 mm/yr) close to pure Zn, which were significantly lower than those of Mg and AZ91HP alloys. As a breakthrough, Bowen et al. [26, 27] examined the corrosion behavior of pure Zn for the first time and found that 1) Zn exhibited excellent biocompatibility after resided in the arterial lumen of Sprague-Dawley rats for 6.5 months; 2) the corrosion products are not potentially hazardous like those of iron; 3) the corrosion rate in the first 2–3 months is very close to the ideal degradation rate for medical implants (0.02 mm/y) [28] and followed by an acceleration in 3–6 months; 4) a uniform corrosion is detected in earlier months so that the corrosion is more or less uniformly distributed over the entire exposed surface and the corrosion proceeds at approximately the same rate over the exposed metal surface [29]. All these corrosion characteristics of pure Zn suggest that Zn arterial corrosion behavior may be superior to other explored materials in the

AMS field [24, 27]. The major concern for a pure Zn stent is that the tensile strength is relatively low (80 – 120 MPa). Stent materials used to prop open the lumen of arteries needs to have a tensile strength of at least 200 MPa, preferably close to 300 MPa [30]. Improvements in mechanical properties of Zn can be obtained through manipulation of its microstructure [31, 32] or alloying [25]. Our previous studies [33] on the Zn-Li system indicated that the incorporation of Li into Zn would increase the ultimate tensile strength (UTS) from < 120 MPa (pure Zn) to > 560 MPa (6 at% Li). However, a too high content of Li lowers the ductility significantly due to the larger volume fractions of the $LiZn_4$ phase. To maintain applicable ductility and sufficient strength for the cardiovascular stent application, the addition of Li should remain below 4 at.%.

Novel Zn-3Li alloy wires (with 3 at.% of Li) were prepared in this study. Metallurgical characterizations, *in vivo* biodegradation and *in vivo* biocompatibility analysis of the Zn-3Li wire were carried out. The present body of work aimed at retaining the outstanding corrosion behavior yet improving the mechanical and corrosion uniformity characteristics.

2. Materials and methods

2.1 Materials

Pure Zn (99.99 wt.%, Alfa Aesar company, Ward Hill, MA) and pure Li foil (99.9 wt.%, Alfa Aesar company, Ward Hill, MA) were loaded into a graphite crucible in an inert-atmosphere glove box to avoid atmospheric oxidation of lithium. A custom vacuum induction melting setup at Michigan Tech was used to fabricate the Zn-Li alloys. They were cast by induction melting with a power of ≈ 3 kW under a 0.9 atm argon atmosphere. The ultimate vacuum level was 2×10^{-4} torr. A stepper motor controlled by a custom LabView (National Instruments, Austin, TX) script tilt-poured the melt into a 25 mm diameter stainless steel mold. 4N Zn wire (99.99 wt.%, Goodfellow Corporation, Oakdale, Pennsylvania) was utilized as control samples.

2.2 Manufacture of Zn-3Li wires

The Zn-3Li alloy was further processed following a hot extrusion process employing a 10 MN extruder (SMS MEER GmbH). Prior to the extrusion, the Zn-3Li billets possessing a diameter of 25 mm were heated to a temperature of 200°C and the extruder's recipient was heated to 210°C. In order to reduce the extrusion ratio, a die with four 0.5 mm in diameter openings was used for extrusion. Extrusion of the billets was carried out with a ram velocity of 0.1 mm/s (F_{max} = 4.1 MN) resulting in four Zn-3Li rods, each with a diameter of 0.5 mm. The overall extrusion ratio was determined to be 2500. Cooling of the rods was allowed at RT.

Subsequent wire drawing was carried out at a temperature of 180°C by means of a self-constructed drawing machine at Leibniz Universität Hannover. Multiple drawing passes were used to reduce the wires' diameters to 0.25 mm. The drawing dies opening diameters used for the drawing sequence were: 0.477 mm, 0.435 mm, 0.362 mm, 0.330 mm, 0.274 mm and 0.250 mm. Annealing or other heat treatment procedures were not required between the particular drawing passes.

2.3 Material characterizations

Inductively Coupled Plasma Optical Emission Spectrometry (ICP-OES) (PerkinElmer Optima 7000DV, Waltham, MA) was utilized in detecting the compositions of Zn alloy wire after drawing. To produce a solution suitable for ICP-OES analysis, 80 mg of alloy wire was dissolved in 12 ml of 6M HCl, which was diluted for analysis.

The Zn-3Li sections were positioned in epoxy in order to obtain both the longitudinal (parallel to the extrusion or rolling direction) and transverse (perpendicular to the extrusion or rolling direction) view of each material. Mounted wires were polished with 600-grit, 800-grit, and 1200-grit silicon carbide. Final polishing steps were performed using 6 μm, 1 μm and 0.1 μm diamond cloth and 0.05 μm alumina slurry on microfiber. Microstructure of alloys were recorded using a Leica EC3 (Leica Microsystems; Buffalo Grove, Illinois) digital camera on an Olympus PMG-3 metallograph (Olympus, Shinjuku, Tokyo, Japan).

The polished wire sections were also carbon-coated and imaged with a JSM 6400 scanning electron microscope (SEM) (JEOL, Peabody, MA). The accelerating voltage and working distance used for SEM were 15 kV and 39 mm. Elemental contrast from the alloy surface was assessed from the collected backscattering electrons.

X-ray diffraction (XRD) was performed on an XDS2000 θ/θ X-ray diffractometer (Scintag Inc., Cupertino, CA) with CuKα radiation (λ = 1.540562 Å). The scans were performed continuously from 35° to 45° in 2θ at a speed of 0.2°/min with a step size of 0.02°. Uniaxial tensile tests were performed using a Bose ELF 3200 mechanical tester (Bose Inc., MN, US). Prior to the test, wires were mounted on two polycarbonate (PC) holders using Loctite General Purpose epoxy (Henkel Corporation; Westlake, OH). The gauge length was set to be 10 mm. A small load cell (max. load: 22.2 N) was used, and the relative displacement and the strain rate were 12mm and 0.01 mm/sec. Yield stress, tensile stress, elongation to failure were calculated from the stress-strain curves. Standard deviation was estimated from eight 4N Zn and five Zn-Li wires. The ductility in % area reduction was also estimated by measuring the area reduction at the fracture based on four different wires.

Vickers microhardness (HV) was measured using an M-400-G1 digital hardness tester (LECO, St Joseph, MI) at a load of 200 g for 5 s and 18 indentations per sample. Standard deviation was estimated from eighteen different points from the longitudinal section of a 4N Zn and a Zn-Li wire.

Volume fraction and average particle size were determined using the ImageJ software. The volume fraction of precipitation phase was calculated as the sum of areas of all black particles divided by the total area of the image. The average area of precipitates was calculated as the sum of the area of precipitates divided by number of particles. The average particle size was calculated from this average area assuming spherical geometry.

2.4 Arterial implantation

The primary method of this *in vivo* evaluation was based on a Sprague Dawley rat (Harlan Labs) model [34]. All animal tests have been approved by the animal care and use committee (IACUC) of Michigan Technological University. 4N Zn and Zn-3Li alloy wire

samples with diameter of 0.25 mm and length of 2 cm were punched into the abdominal aorta and then directed into the lumen for 10 mm before exteriorization. In this case, wires were immersed in the flowing blood to mimic the environment of a stent strut. After 2–12 months, rats were euthanized and rat aortas containing the wire implants were harvested. The wires had not become dislocated from their implant location at the time of collection. To preserve the corrosion layer, explanted wires were preserved in 200 proof ethanol.

2.5 Biodegradation analysis

Part of the corroded wires were mounted in epoxy and cut transversely to expose the cross section. Wire mounts were ground with 800 grit SiC, 1200 grit SiC, 6 μm diamond and 1 μm alumina and then cut into slices with thickness of 1 mm to fit into an aluminum mount with carbon tape. The wire cross section was coated with thin layer of carbon before imaging with the scanning electron microscope. Imaging of the wires was conducted at 15 kV accelerating voltage with a reduced working distance of 12 mm using a backscattered detector. Cross sectional area (CSA) analysis of the backscattered image were conducted using ImageJ software (Fig.5a) [35]. The penetration rate was determined according to the following equation:

$$Penetration\ rate\ (\mu m/yr) = \frac{\sqrt{\frac{Nominal\ CSA}{\pi}} \sqrt{\frac{Metallic\ CSA}{\pi}}}{\frac{Corrosion\ Time}{360}}$$

Elemental mappings of Ca, P, C, Cl, Zn, O from cross sections were captured to signify the corrosions using an environmental scanning microscope (FEI Philips XL 40). The accelerating voltage and working distance were 15 kV and 10 mm.

FT-IR was conducted in diffuse reflectance mode with a Jasco FTIR-4200 spectrophotometer. A series of 64 scans were performed at 4 cm^{-1} resolutions from 800 to 2000 cm^{-1}.

2.6 Histological evaluation

The leftover wires with aortas were snap-frozen in liquid nitrogen and cryo-sectioned for histological analysis [34]. Before staining, samples were preserved in a −80 °C freezer. Cross sections were ethanol fixed and then stained with hematoxylin and eosin (H&E), mounted in Permount solution and imaged using an Olympus BX51, DP70 bright-field microscope. The neointimal tissue with smooth muscle cells and inflammatory cells were inspected around the implants; variations of cell densities in the artery wall, lumen interface and biocorrosion area were measured.

2.7 Statistical analysis

All quoted errors and error bars correspond to the sample standard error.

3. Results

3.1 Material characterizations

Experimental compositions of the alloys are given in Table 1. For this Zn-Li alloy, the experimental composition for Li is 3 at.%. Cu, Mg, Fe and Pb were detected as trace impurities from Zn; and Cd, Al and Ni remained below the detection limit for the three alloys.

Surface images in Fig. 1(a, c) exhibited severe rolling texture and precipitates. The darkest phase (representing the lowest atomic number) from the BSE images in Fig.1(b, d) indicate the occurrence of spherical and ribbon-like precipitates. This could be the Li-rich phase.

Fig. 2 illustrates the optical microstructure, back-scattering electron imaging and XRD result for the extruded Zn-3Li wires. The longitudinal sections of the Zn-Li alloy after drawing attained a preferential orientation at an angle of 27° with the extrusion direction. The transverse sections exhibited two main phases. The bright phase is the Zn rich matrix and the dark phase corresponds to Li rich precipitates, formed in the eutectic reaction. This is consistent with the BSE images in Fig. 2(d). The darkest precipitate phase (Li-rich phase) possessed the lowest average atomic number. The volume fraction and average particle size determined from the ImageJ software was 51 ± 3% and 1.1 ± 0.3 μm, respectively.

The XRD result in Fig. 2(e) indicates that the two phases from the micrographs are the zinc phase (43.24° and 39.02°) and the minor phase is $LiZn_4$ (41.20° and 42.96°). For the intermetallic $LiZn_4$ phase, the highest relative intensities of peaks came from the crystallographic plane sets of {002}. According to Pearson's Crystal powder pattern for $LiZn_4$ (No. 1321631), the strongest peak should be (101). This inconsistency could be due to the preferred orientation along (002) exerted from the extruding process.

Table 2 summarizes the mechanical properties of Zn-Li wires compared with the 4N Zn wire. It should be noted that Zn-3Li exhibited higher yield strength, tensile strength, hardness and lower ductility than 4N Zn.

The representative tensile stress curve (Fig. 3b) shows that the zinc alloy endured a significant plastic deformation and necking before fracture occurred. The curve indicates an ultimate tensile stress of 220 MPa and an elongation to failure of 24%. The average strength values from the five Zn-Li wires increased by over 100% relative to 4N Zn and the ductility in percent of elongation was also retained at 17%, reaching the minimum mechanical requirement for a stent [36]. The increase in strength could be due to the large volume fractions of the $LiZn_4$ phase for the alloy wires. SEM examination of the fracture surface (Fig. 3c, d) revealed a clear necking shrinkage and dimpled surface, indicating a moderately ductile behavior for the Zn alloy. The spherical "dimples" corresponding to microvoids are believed to initiate the crack formation.

3.2 *In vivo* corrosion analysis

From the backscattered electron images (BSE), both the remaining metallic sections (shown as the lighter phase) and the mixture of corrosion products, the epoxy and tissue (shown as

the darker phase) were detected. Dark areas inside the boundaries of explant cross sections indicated a lower atomic number corrosion product made of zinc oxide, as will be demonstrated later by x-ray maps. BSE images recorded after different periods of the alloy wire explants (Fig. 4a) indicated the loss of the circular wire integrity after 2 months of *in vivo* degradation. It progressed further until 12 months.

Elemental maps of the same series of cross sections revealed the presence of the following major elements: Zn, Ca, P, O, C and Cl (Fig. 4c). At 2 months, a Ca and P-containing exterior layer was detected adjacent to the inner layer containing Zn, C and O. A variation in distribution of the corrosion products containing those elements is apparent from elemental maps in Figure 4a. The outermost layer consists mainly of Ca and P, and the thin layer adjacent to the metallic leftover is enriched with Cl, O and Zn, followed by a tiny content of C in particular regions. The distributions of Ca and P are almost identical, indicating the presence of a more uniform layer of

CaP at 2 months. This is in a disparity to what was reported for the Mg wire [37], where Ca was incorporated in a more outer layer than P. At 4 months, apart from the more evident loss of the metallic area, wire cross sections are surrounded by ceramic layer composed of Ca and P elements, which thickness appears to be more uniform around perimeter. The higher content of C at 4 months is believed to be related to the penetration of epoxy into the oxide corrosion product, and not result of the corrosion. This conclusion is in agreement with the contrast for the BSE image.

As shown in Fig. 4, the distribution of Cl is similar to Zn. The high intensity Cl spot is aligned with O, indicating the possible corrosion product of Zn-O-Cl. At 6.5 months, both the CaP layer and the Zn-O layer thickened and the C signals started to appear in some inner regions adjacent to O and Zn. This suggests the onset of the formation of Zn-O-C at 6.5 months. At 9 months, the coverage and distribution of all elements of interest around metallic implant suggest increased amount of corrosion products, especially Zn-O-C. Approximately 1/5 of the inner Zn area was lost at 12 months. The corrosion layer of Zn-O segregated in the locations where most corrosion occurred. The layers of CaP and Zn-O-C did not increase significantly as compared to the previous stage. The nearly identical distribution of the Cl and Zn elements and the overlap between O and Cl in the enlarged island area provide evidence for formation of Zn-O-Cl product(s) at 12 months.

FT-TR (infrared spectroscopy) was used to substantiate the surface products present on explanted Zn alloy wires. In the FT-IR spectrum (Fig. 4b), a narrow and high intensity PO_4^{3-} band is observed at 1050–1180 cm^{-1}, which is related to the asymmetric stretching of the $\nu 3$ group [38]. The absorption band in the range of 920–1000 cm^{-1} is characteristic of the symmetrical stretching of the $\nu 1$ group [39]. The CO_3^{2-} bands from the $\nu 3$ apatitic substitution were detected at 1390–1500 and 1540–1620 cm^{-1} [40, 41].

Based on the signature of Zn, O, Ca, P, C from elemental map and the presence of PO_4^{3-} and CO_3^{2-} from FT-IR, it is assumed that the compact degradation product of Zn-Li consisted of an inner Zn-O layer, followed by Zn-Cl-O, zinc carbonate ($ZnCO_3$) and a calcium phosphate (CaP) layer. Another possible corrosion product, $Zn_3(PO_4)_2{\cdot}2H_2O$, which

is a more thermodynamically stable mineral at physiological pH [42] were absent based on the lack of spatial overlapping between the elements Zn and P. This may either indicate that the formation of $Zn_3(PO_4)_2{\cdot}2H_2O$ in this system needs longer time or that the local pH had increased to above the physiological state due to the corrosion reaction: $Zn+O_2+H_2O = Zn^{2+}+4OH^-$.

Cross-sectional analysis showed an incremental increase of the degradation rate for Zn-Li alloy during the implantation from 2 to 12 months. A moderate low degradation rate of 0.08 to 0.016 mm/yr was observed at 2 to 4 months. The earlier degradation for the alloy wire was a little slower than that of 4N Zn and the benchmark for the ideal degradation (0.02 mm/y) of medical implants [28]. However, the degradation of Zn-Li alloy accelerated to 0.019 mm/yr at 9 months and 0.046 mm/yr at 12 months, which is twice as high as that of the 4N Zn sample (Fig. 5b). This acceleration in later stage is preferred since the stent would dissolve quickly in the body after the supporting function has ceased. Fig. 5c demonstrates the percent of cross sectional area reduction for 4N Zn and the Zn-Li alloy over implantation time. The dashed line corresponds to the targeted cross area reduction of 20 μm/yr reported earlier [28].

The corroded area for Zn-Li was a little less than for 4N Zn before 9 months and increased thereafter, which is consistent with the penetration rate results shown in Fig. 5b. Both 4N Zn and Zn-Li followed almost the same trend with the targeted value and retained about 70% of the original area after 12 months *in vivo*. The identical loss of area for 4N Zn and Zn-Li over 12 months indicates the very similar average corrosion rate for the two materials. Surprisingly, the Zn-Li curve displayed a near-liner relationship ($R^2 = 0.99$) between the percent of area reduction and time, and the slope of the curve ($k = 2.63$) was much closer to the target value ($k = 2.67$). This suggests a near ideal uniform gradual acceleration of biodegradation for this alloy.

3.3 *In vivo* biocompatibility analysis

Fig. 6 also shows two areas of interest at higher magnification for the 11 month luminal explants. Panels C and D demonstrate regions of chronic inflammation within the red circle that correspond to the green asterisks on panels A and B.

In panel E, the blue asterisk identifies a media layer largely devoid of smooth muscle cells, while panel F identifies a neo-intima largely populated with cells. These areas corresponded to the red asterisks on panels A and B. It should be noted that the media layer for the Zn-3Li specimen appears largely deteriorated closer to the implant. Wide open arterial lumens and low neointimal growth around the implant is evident from the images and indicates excellent biocompatibility for Zn-Li, although inflammation and neointima thickness appear to be slightly higher for Zn-Li relative to 4N Zn.

4. Discussions

4.1 The role of Li on the corrosion rate of Zn

It is known that alloying a second element into a metallic structure may not only change the mechanical properties but also modify the corrosion behavior. In the Zn-Li alloys, based on

the optical micrographs and XRD results, it is assumed that element Li existed partly in solid solution but also precipitated in the form of $LiZn_4$ as part of an eutectic structure.

As shown schematically in Fig. 7, there are two sources of galvanic corrosion in this system: one is between the Zn-matrix and $LiZn_4$ and the other is between the eutectic-Zn and $LiZn_4$. Due to the potential difference of the two, the precipitated secondary phase $LiZn_4$, which is nobler than Zn, can accelerate the corrosion of the matrix due to micro-galvanic corrosion. However, the comparison of the penetration rates in Fig. 5(b) showed that the Zn-Li alloy corrodes slower than 4N Zn in the early stage. This can be explained as follows: the volume fraction of the $LiZn_4$ phases as determined using the ImageJ software is up to 51 ± 3%. During the corrosion processes these large amounts of precipitates could act as an anodic barrier and an enrichment of the corrosion product to inhibit the overall corrosion rate of the alloy. Therefore, the formation of the $LiZn_4$ phase in this alloy contributes to a slower corrosion of the Zn-Li alloy. The decrease of the susceptibility to atmospheric corrosion resulting from alloying with Li was also detected in Mg-12 at.% Li [43]. Moreover, the molar ratio of $LiZn_4$ to the adjacent eutectic-Zn for Zn-3Li was 40% (calculated from the Zn-Li phase diagram) and this may also influence the galvanic cells. Apart from the high volume fraction effect, the aggregates of the corrosion layers from the uncorroded intermetallic $LiZn_4$ phase, together with other corrosion coatings consisting of zinc oxide, perchlorate, carbonate and calcium phosphate layers also retarded the corrosions. However, this decrease of the susceptibility to atmospheric corrosion from large volume fractions of $LiZn_4$ can be undermined with the progression of corrosion, as evidenced by the drastic increase of the corrosion rate for the alloy wire after 9 months. This can be due to the dissolution of the passive film and the incorporation of dissolved oxygen, ions or other proteins and cells. In this way, the structure of the passive film will loosen and the previous initiated pits may spread, which promotes a rapid attack of the bulk metal [44].

4.2 Corrosion mechanism

The production of the corrosion products in this system were estimated based on the Pourbaix diagram of Zn-Li-H_2O at 37°C (calculated using FactSage 7.0 software).

All of the thermodynamic equilibrium equations of Zn and Li with the physiological ions present in H_2O are shown in Fig. 8. Zn-Li-H_2O and Zn-Li-X-H_2O diagrams are shown for X = {C, P, Cl} and $[Zn^{2+}, Li^{+}]=\{10^{-6}\}$. To mimic the *in vivo* corrosion environment, concentrations for Cl^{-}, HPO_4^{2-} and HCO_3^{-}(CO_2(aq)) in this diagram were set to be identical to the values in human blood plasma (0.1 mol/L for Cl^{-}, 0.001 mol/L for HPO_4^{2-}, and 0.027 mol/L for CO_2(aq)) [45]. In the Zn-Li-H_2O system, at low potentials of $E < -1.4$ V, both Zn and Li are in the immunity region and thus stable in their metallic form. As Li possesses higher activity than Zn, with potential increases, Li would be oxidized first. If surface potential E is over −0.8 V, and at pH < 8.3, both Zn and Li would go into solution. The Pourbaix diagram also shows that both the Zn^{2+} and Li^{+} are stable at low pH; the oxide, ZnO, at intermediate pH; and the ZnO and LiOH at very high pH.

The Pourbaix diagram is assumed to represent the thermodynamic equilibrium conditions. On a contrary, in a real corrosion situation, the local pH values in the cathodic and anodic areas are always higher and smaller, respectively, than at equilibrium. Therefore, the red

circles marked on the Pourbaix diagrams in Figure 8 which stand for physiological conditions with tissue fluid (pH ≈ 7.4 and $E \approx 0.78$ V) [46]. At pH ≈7.4, the Zn-Li-C-H_2O system reaches the equilibrium with $ZnCO_3$ and ZnO as the corrosion product. In the diagram of Zn-Li-P-H_2O, it is believed that Zn_3P_2 only exists if the potential is in the range of −0.7 V < E < −0.6V. At physiological potential, Zn_3P_2 dissolves and ZnO becomes the only solid product. No $Zn_3(PO_4)_2{\cdot}2H_2O$ was detected under all conditions. From the elemental mapping in Fig. 4a, there was still a signal for a Zn-Cl-O mineral. However, in the Zn-Li-Cl-H_2O system, no solid Zn-Cl-O products were suggested around the potential of the tissue fluid. It is possible that the as-formed chloride product was not stable at pH = 7.4. $Zn_5(OH)_8Cl_2{\cdot}H_2O$, which can be formed due to the reaction of $ZnCl_2$ with ZnO only exists at a pH of 6.9. Furthermore, after implantation, apart from the contact with Cl^-, HCO_3^-, HPO_4^{2-}, the Zn-Li alloy implants were also exposed to an environment rich in blood, protein, cations (Na^+, K^+, Ca^{2+}, Mg^{2+}, etc.), organic substances of low-molecular-weight species, polymeric components of high molecular-weight, as well as dissolved oxygen [47]. This physiological environment makes the corrosive medium extremely complex, which can alter the properties of corrosion products and corrosion rates [46].

Based on the Pourbaix diagram, the following degradation sequence of the Zn-Li alloy in a physiological environment is assumed: when Zn-Li is exposed to the aqueous solutions, it shows some hydrogen gas evolution (Eq. 1), which is balanced by dissolution of Zn (Eq. 2). As dissolution progresses, the pH increases with the formation of OH^- from the cathodic reaction, which promotes the production of ZnO according to the Pourbaix diagram. Along with the deposition of a passive ZnO layer (Eq. 3), the existence of HCO_3^- (Eq.4), Cl^-(Eq.5) and HPO_4^{2-} (biomineralization from the introduction of calcium) in the body fluid also favors thermodynamically the formation of new phases. The passive film would thus be reconstructed into layers of zinc oxide, zinc chloride hydroxide, zinc carbonate and calcium phosphate layer.

$$2H_2O+2e^-=H_2+2OH^- \text{ (cathodic reaction)} \quad (1)$$

$$Zn(s)=Zn^{2+}(aq)+2e^- \text{ (anodic reaction)} \quad (2)$$

$$\begin{gathered} Zn^{2+}+2OH^-=Zn(OH)_2=ZnO+H_2O \text{ (product formation)} \\ H_2O+CO_2=H_2CO_3=HCO_3^-+H^+ \end{gathered} \quad (3)$$

$$Zn^{2+}+2HCO_3^-=ZnCO_3+H_2 \text{ (product formation)} \quad (4)$$

$$Zn^{2+}+2Cl^{-}+4ZnO+5H_2O=Zn_5(OH)_8Cl_2\cdot H_2O\,(\text{product formation}) \quad (5)$$

5. Conclusions

A new Zn-3Li alloy has been cast, extruded and analyzed for biomedical-focused applications. XRD results indicated the formation of $LiZn_4$ through the emergence of diffraction peaks corresponding to (002) and (101) for this phase. Mechanical testing showed that alloying of Zn with 3 at.% of Li increased the tensile strength from 116 ± 13 MPa (pure Zn) to 274 ± 61 MPa while the ductility was still being held at 17 ± 7%.

The elemental mapping and FT-IR analysis jointly confirmed that the corrosion products are calcium phosphate, zinc oxide, zinc chloride hydroxide and zinc carbonate. The quantitative corrosion analysis showed a moderate low degradation rate of 0.019 mm/yr at 6.5 months that increased to 0.046 mm/yr at 12 months. This later stage acceleration is beneficial in that the stent would dissolve quickly in the body after the scaffolding function ceased around 6 months. The corroded volume for Zn-3Li was only slightly smaller than that of 4N Zn at 6 months but both of them retained about 70% of their original dimensions after 12 months *in vivo*. The nearly identical oxidation progression for 4N Zn and Zn-Li indicates a very similar corrosion rate for the two materials. Moreover, the cross sectional area reduction curve for Zn-Li displayed a near-liner relationship between the percent of area reduction and time. This suggests a near ideal uniform gradual acceleration of biodegradation for this alloy. Biocompatibility results for the Zn-Li alloy at 11 months *in vivo* indicated a moderate inflammation with a non-obstructive neointima.

All the preliminary results obtained from implantation in rat abdominal arteries demonstrated that this new Zn-Li alloy is another promising biodegradable coronary stent material based on its improved mechanical properties and the outstanding corrosion behavior as compared to pure Zn.

Acknowledgments

U.S. National Institute of Health-National Heart, Lung, and Blood Institute (Grant #1R15HL129199-01) and U.S. National Institute of Health-National Institute of Biomedical Imaging and Bioengineering (Grant #5R21 EB 019118-02) are acknowledged for funding this study. The authors thank Dr. Jianfeng Jiang from Biomedical Department of Michigan Technological University for the mechanical tester, Mingxiao Ye from Physics Department of Michigan Technological University for the FT-IR test and Dr. Timothy Eisele from Chemical Engineering of Michigan Technological University for the Factsage software support. The authors also thank the staff of the Applied Chemical and Morphological Analysis Laboratory for assisting with the sample preparation for electron imaging.

References

1. Zheng YF, Gu XN, Witte F. Biodegradable metals. Mater Sci Eng Reports. 2014; 77:1–34.
2. Moravej M, Mantovani D. Biodegradable metals for cardiovascular stent application: interests and new opportunities. Int J Mol Sci. 2011; 12:4250–4270. [PubMed: 21845076]
3. Heublein B, Rohde R, Kaese V, Niemeyer M, Hartung W, Haverich A. Biocorrosion of magnesium alloys: a new principle in cardiovascular implant technology? Heart. 2003; 89:651–656. [PubMed: 12748224]

4. Hascoët S, Baruteau A, Jalal Z, Mauri L, Acar P, Elbaz M, Boudjemline Y, Fraisse A. Stents in paediatric and adult congenital interventional cardiac catheterization. Arch Cardiovasc Dis. 2014; 107:462–475. [PubMed: 25128078]
5. Colombo A, Karvouni E. Biodegradable stents: "fulfilling the mission and stepping away". Circulation. 2000; 102:371–373. [PubMed: 10908206]
6. Erne P, Schier M, Resink TJ. The road to bioabsorbable stents: reaching clinical reality? Cadiovasc Intervent Radiol. 2006; 29:11–16.
7. Saito S. New horizon of bioabsorbable stent. Catheterization and cardiovascular interventions: official journal of the Society for Cardiac Angiography & Interventions. 2005; 66:595–596. [PubMed: 16284981]
8. Saris NE, Mervaala E, Karppanen H, Karppanen H, Khawaja JA, Khawaja Ja, Lewenstam A. Magnesium. An update on physiological, clinical and analytical aspects. Clin Chim Acta. 2000; 294:1–26. [PubMed: 10727669]
9. Cheng J, Zheng YF. In vitro study on newly designed biodegradable Fe-X composites (X = W, CNT) prepared by spark plasma sintering. J Biomed Mater Res Part B. 2013; 101:485–497.
10. Seitz JM, Lucas A, Kirschner M. Magnesium-Based Compression Screws: A Novelty in the Clinical Use of Implants. JOM. 2016; 68:1177–1182.
11. Kirkland NT, Lespagnol J, Birbilis N, Staiger MP. A survey of bio-corrosion rates of magnesium alloys. Corros Sci. 2010; 52:287–291.
12. Mueller WD, Lucia Nascimento M, Lorenzo de Mele MF. Critical discussion of the results from different corrosion studies of Mg and Mg alloys for biomaterial applications. Acta Biomater. 2010; 6:1749–1755. [PubMed: 20051271]
13. Zhang E, Yang L. Microstructure, mechanical properties and bio-corrosion properties of Mg Zn Mn Ca alloy for biomedical application. Mater Sci Eng A. 2008; 497:111–118.
14. Hort N, Huang Y, Fechner D, Störmer M, Blawert C, Witte F, Vogt C, Drücker H, Willumeit R, Kainer KU, Feyerabend F. Magnesium alloys as implant materials – Principles of property design for Mg RE alloys. Acta Biomater. 2010; 6:1714–1725. [PubMed: 19788945]
15. Peng Q, Huang Y, Zhou L, Hort N, Kainer KU. Preparation and properties of high purity Mg Y biomaterials. Biomaterials. 2010; 31:398–403. [PubMed: 19800117]
16. Liu B, Zheng YF. Effects of alloying elements (Mn, Co, Al, W, Sn, B, C and S) on biodegradability and in vitro biocompatibility of pure iron. Acta Biomater. 2011; 7:1407–1420. [PubMed: 21056126]
17. Liu B, Zheng YF, Ruan LQ. In vitro investigation of $Fe_{30}Mn_6Si$ shape memory alloy as potential biodegradable metallic material. Mater Lett. 2011; 65:540–543.
18. Yusop AH, Bakir AA, Shaharom NA, Abdul Kadir MR, Hermawan H. Porous biodegradable metals for hard tissue scaffolds: a review. Int J Biomater. 2012; 2012:1–10.
19. Ge Q, Dellasega D, Demir AG, Vedani M. The processing of ultrafine-grained Mg tubes for biodegradable stents. Acta Biomater. 2013; 9
20. Li H, Zheng Y, Qin L. Progress of biodegradable metals. Prog Nat Sci: Mater Int. 2014; 24:414–422.
21. Narayanan, TSNS., Park, I-S., Lee, M-H. Surface modification of magnesium and its alloys for biomedical applications: Opportunities and challenges, Surface Modification of Magnesium and its Alloys for Biomedical Applications. Woodhead Publishing; Oxford: 2015. p. 29-87.
22. Chu, PK., Wu, GS. Surface design of biodegradable magnesium alloys for biomedical applications, Surface Modification of Magnesium and its Alloys for Biomedical Applications. Woodhead Publishing; Oxford: 2015. p. 89-119.
23. Tapiero H, Tew KD. Trace elements in human physiology and pathology: zinc and metallothioneins. Biomed Pharmacother. 2003; 57:399–411. [PubMed: 14652165]
24. Bowen PK, Shearier ER, Zhao S, Guillory RJ Ii, Zhao F, Goldman J, Drelich J. Biodegradable Metals for Cardiovascular Stents: from Clinical Concerns to recent Zn-Alloys. Adv Healthc Mater. 2016; 03:1–20.
25. Vojtech D, Kubasek J, Serak J, Novak P. Mechanical and corrosion properties of newly developed biodegradable Zn-based alloys for bone fixation. Acta Biomater. 2011; 7:3515–3522. [PubMed: 21621017]

26. Bowen PK, Guillory RJ Ii, Shearier ER, Seitz J-M, Drelich J, Bocks M, Zhao F, Goldman J. Metallic zinc exhibits optimal biocompatibility for bioabsorbable endovascular stents. Mater Sci Eng C. 2015; 56:467–472.
27. Bowen PK, Drelich J, Goldman J. Zinc exhibits ideal physiological corrosion behavior for bioabsorbable stents. Adv Mater. 2013; 25:2577–2582. [PubMed: 23495090]
28. Atrens, MLA., Zainal Abidin, NI., Song, G-L. Corrosion of magnesium alloys, Corrosion of magnesium (Mg) alloys and metallurgical influence. Woodhead Publishing; Philadelphia, PA, USA: 2011. p. 153
29. Jones, DA. Principles and prevention of corrosion. Macmillan Publishing Co; New York, NY: 1996. p. 142-147.
30. Werkhoven, RJ., Sillekens, WH., van Lieshout, JBJM. Processing Aspects of Magnesium Alloy Stent Tube. Magnesium Technology, John Wiley & Sons, Inc; 2011. p. 419-424.
31. Zhang X, Yuan G, Wang Z. Mechanical properties and biocorrosion resistance of Mg-Nd-Zn-Zr alloy improved by cyclic extrusion and compression. Mater Lett. 2012; 74:128–131.
32. Kang F, Liu JQ, Wang JT, Zhao X. Equal Channel Angular Pressing of a Mg 3Al 1Zn Alloy with Back Pressure. Adv Eng Mater. 2010; 12:730–734.
33. Zhao S, McNamara CT, Bowen PK, Verhun N, Braykovich JP, Goldman J, Drelich JW. Structural characteristics and in vitro biodegradation of a novel Zn-Li alloy prepared by induction melting and hot rolling. Metall Mater Trans A. 2016 Under review.
34. Pierson D, Edick J, Tauscher A, Pokorney E, Bowen P, Gelbaugh J, Stinson J, Getty H, Lee CH, Drelich J, Goldman J. A simplified in vivo approach for evaluating the bioabsorbable behavior of candidate stent materials. J Biomed Mater Res, Part B. 2012; 100B:58–67.
35. Abramoff MD, Magalhaes PJ, Ram SJ. Image Processing with ImageJ. Biophotonics Intern. 2004; 11:36–42.
36. Werkhoven, RJ., Sillekens, WH., van Lieshout, JBJM. Processing Aspects of Magnesium Alloy Stent Tube. Magnesium Technology, John Wiley & Sons, Inc; 2011. p. 419-424.
37. Bowen PK, Drelich J, Goldman J. Magnesium in the murine artery: Probing the products of corrosion. Acta Biomater. 2014; 10:1475–1483. [PubMed: 24296127]
38. Frost RL, Martens W, Williams PA, Kloprogge JT. Raman and infrared spectroscopic study of the vivianite-group phosphates vivianite, baricite and bobierrite. Mineral Mag. 2002; 66:1063–1073.
39. Holt C, van Kemenade MJJM, Harries JE, Nelson LS, Bailey RT, Hukins DWL, Hasnain SS, De Bruyn PL. Preparation of amorphous calcium-magnesium phosphates at pH 7 and characterization by x-ray absorption and fourier transform infrared spectroscopy. J Cryst Growth. 1988; 92:239–252.
40. Gibson IR, Bonfield W. Preparation and characterization of magnesium/carbonate co-substituted hydroxyapatites. J Mater Sci Mater Med. 2002; 13:685–697. [PubMed: 15348578]
41. Meejoo S, Maneeprakorn W, Winotai P. Phase and thermal stability of nanocrystalline hydroxyapatite prepared via microwave heating. Thermochim Acta. 2006; 447:115–120.
42. Zberg B, Uggowitzer PJ, Loffler JF. MgZnCa glasses without clinically observable hydrogen evolution for biodegradable implants. Nat Mater. 2009; 8:887–891. [PubMed: 19783982]
43. Białobrzeski A, Saja K, Żmudzińska M. Corrosion behaviour of binary Mg-Li alloys for plastic forming. Arch Foundry Eng. 2011; 11:15–20.
44. Drelich AJ, Bowen PK, LaLonde L, Goldman J, Drelich J. Importance of oxide film in endovascular biodegradable zinc stents. Surf Innovations. 2016; 4:133–140.
45. Kokubo T, Takadama H. How useful is SBF in predicting in vivo bone bioactivity? Biomaterials. 2006; 27:2907–2915. [PubMed: 16448693]
46. Cui, FZ., Feng, QL. Biomaterials Science (Chinese Edition). Tsinghua University Press; Beijing, China: 2004. p. 236
47. Ding Y, Wen C, Hodgson P, Li Y. Effects of alloying elements on the corrosion behavior and biocompatibility of biodegradable magnesium alloys: a review. J Mater Chem B. 2014; 2:1912–1933.

Biographies

Shan Zhao

Shan Zhao is currently a PhD Candidate in Department of Material Science and Engineering at Michgan Technological University, co-advised by Dr. Drelich and Dr. Goldman. Before joining Michigan Tech in 2013, Shan received her M.S. in Materials Science from the University of Florida and her B.S in Materials Science and Engineering from the University of Jinan, China. In the past six years, Shan has received rigorous training in processing and testing of biometals, bioglass and magnetite nanoparticles. Currently Shan has authored or coauthored eight papers. One of her co-authored papers of “Biodegradable Metals for Cardiovascular Stents: from Clinical Concerns to Recent Zn-Alloys” has been published in *Advanced Healthcare Materials*.

Jan-M. Seitz

Dr. Seitz has worked at Leibniz Universität in Hannover, Germany, and Michigan Technological University in Houghton, USA with a focus on lightweight materials research and biomedical engineering applications. He developed process chains for resorbable Mg-implant applications such as stents and osteosynthesis applications and high performance alloys for biomedical applications. During an overseas stay at The University of Auckland, Dr. Seitz developed polymer and ceramic based coatings for medical applications. He is currently working as director for research & development and engineering and production at Syntellix AG, Germany. Dr. Seitz has published more than 60 technical papers and patents.

Rainer Eifler

Rainer Eifler studied mechanical engineering at the Leibniz Universitaet Hannover, Germany. After receiving his diploma, he started working as a scientific assistant in the field of biomedical engineering and lightweight construction at the Institut für Werkstoffkunde at Liebniz Universitaet Hannover, Germany. The emphases of his work for the are extrusion of light metals and casting of magnesium based alloys. Rainer Eifler developed special interest in the field of resorbable alloys for biomedical implants. The topic of his PhD thesis is related to the development of a resorbable magnesium alloy with implant-specific mechanical properties.

Hans Jürgen Maier

Prof. Hans Jürgen Maier is the Chair Professor and Director of the Institut für Werkstoffkunde (Materials Science) at Leibniz Universität Hannover. His research interests are in microstructure-property-relationships in advanced metallic materials, ultrafine-grained and nanocrystalline materials, phase transformations and heat treatments of metals, thermomechanical fatigue behavior of materials, and electron microscopy. He has published 285 peer-reviewed scientific papers and 99 other publications. Prof. Maier is Associate Editor to the new ASM International Journal *Shape Memory and Superelasticity: Advances in Science and Technology. He also serves on the Editorial Board for the Materials Research Letters journal.*

Roger Guillory II

Roger Guillory II graduated with his B.S. in Biomedical Engineering from Michigan Technological University in 2016. His research interest as a PhD student in Biomedical Engineering is focused on the biological response to degradable metallic materials used as resorbable scaffolds.

Elisha J. Earley

Elisha J. Earley is an undergraduate researcher in Biomedical Engineering at Michigan Technological University. She is interested in pathology, immunology, biomaterials, and biological responses to biomaterials.

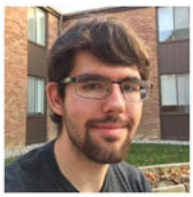

Adam J. Drelich

Adam J. Drelich is an undergraduate student currently studying pharmaceutical science at the University of Michigan College of Pharmacy in Ann Arbor. His current research interests focus on in vitro drug dissolution and prodrug uptake in cancer cells. He has also spent several summers in the past as a research intern at Michigan Technological University working on bioabsorbable arterial stents, from which he has helped author 3 technical publications

Jeremy Goldman

Jeremy Goldman earned his Ph.D. in Biomedical Engineering from Northwestern University in 2002. He joined the Department of Biomedical Engineering at Michigan Technological University in 2004. He earned his B.S. in 1998 from Cornell University, in Chemical Engineering. Dr. Goldman's research interests include the investigation of novel vascular biomaterials, including polymeric, natural, and metallic, for vascular repair and regeneration.

Jaroslaw W. Drelich

Dr. Jaroslaw W. Drelich received his MS degree in chemical technology from the Technical University of Gdansk, Poland, in 1983, and earned his Ph.D. degree in metallurgical engineering from the University of Utah in 1993. He came to Michigan Technological University in 1997 and currently is a professor of materials science and engineering. Aside from teaching several courses on characterization of materials, Dr. Drelich has edited 6 books, published nearly 200 technical papers, holds 9 patents and has more than 60 conference presentations, including several keynote addresses, to his credit. Dr. Drelich is the Editor-in-Chief for the *Surface Innovations Journal*.

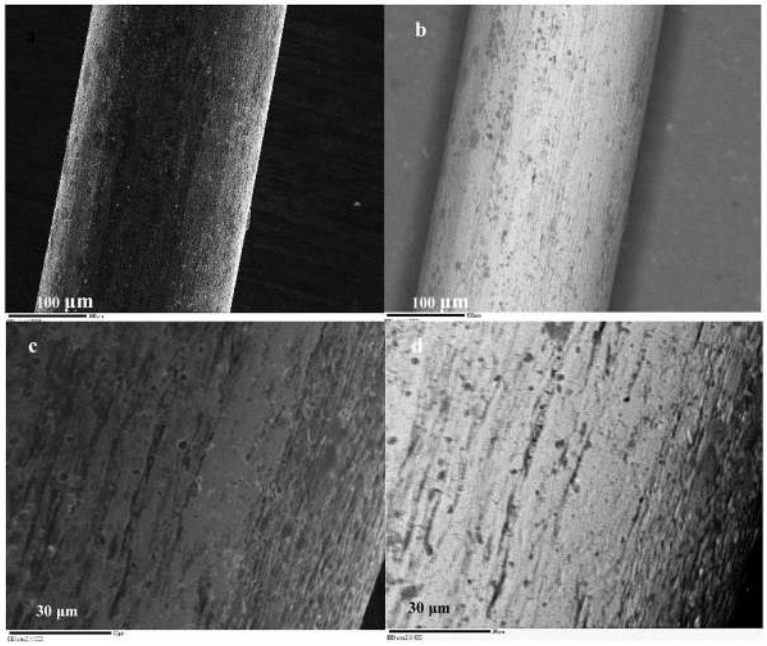

Fig 1.

SEM secondary electron (a, c) and backscattered electron images (b, d) for the as-received Zn-Li wire surface

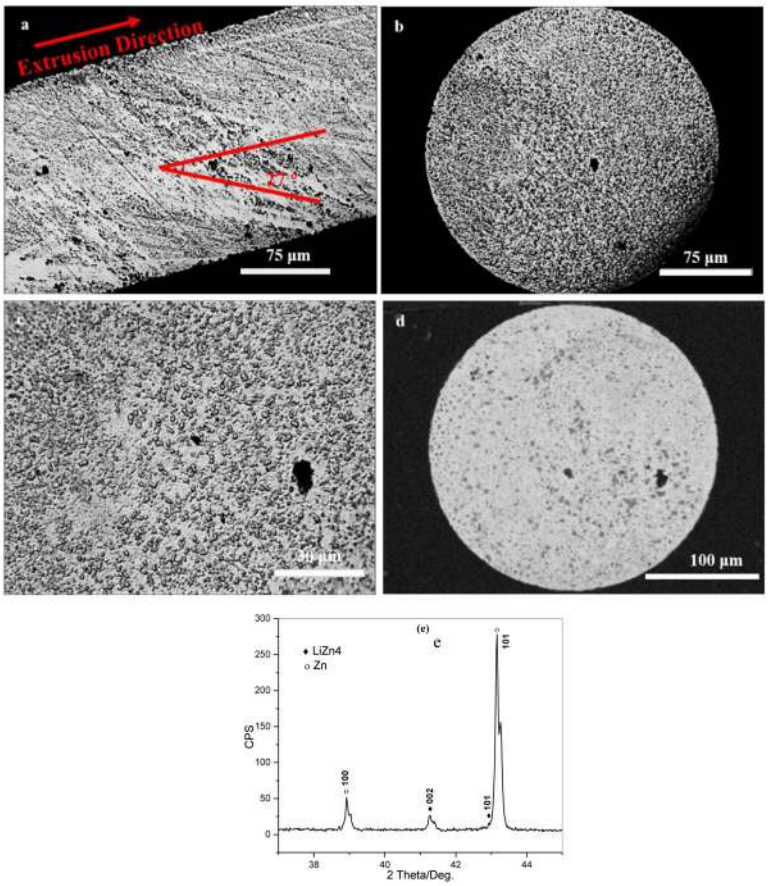

Fig 2.

Optical microscopy images of the Zn-3Li wire (Ø = 0.25 mm) from longitudinal (a), transverse cross sections (b, c), backscattered electron image (d) and X-ray pattern for Zn-3Li (e).

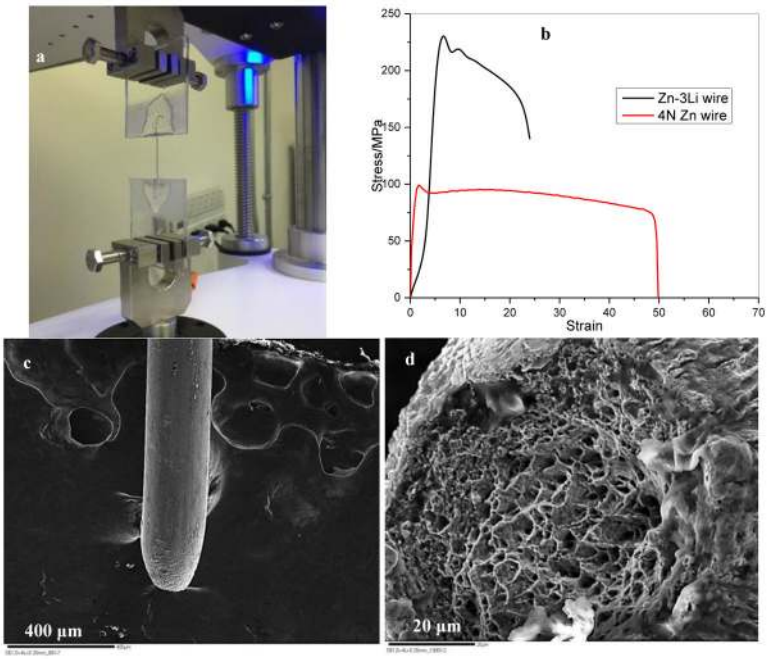

Fig 3.

Set-up for the tensile test (a), representative tensile stress-strain curve of 4N Zn and Zn-3Li (b) and fracture images of Zn-3Li (c,d).

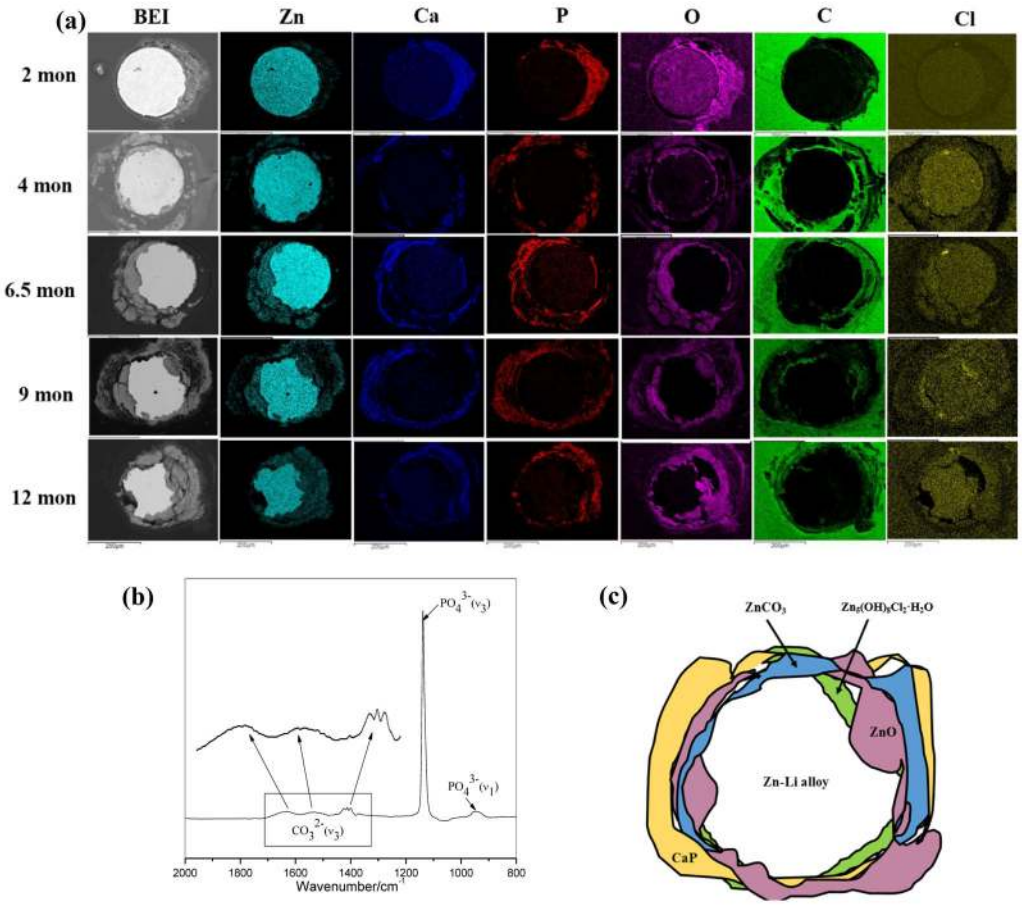

Fig 4.

(a) Backscattered electron images and elemental maps (EDS) of Zn-3Li wire sections after residing in the rat arterial for 2 to 12 months; (b) FTIR spectrum of Zn-3Li wire for 13.5-month residence; (c) Schematic phase map for 9-month residence.

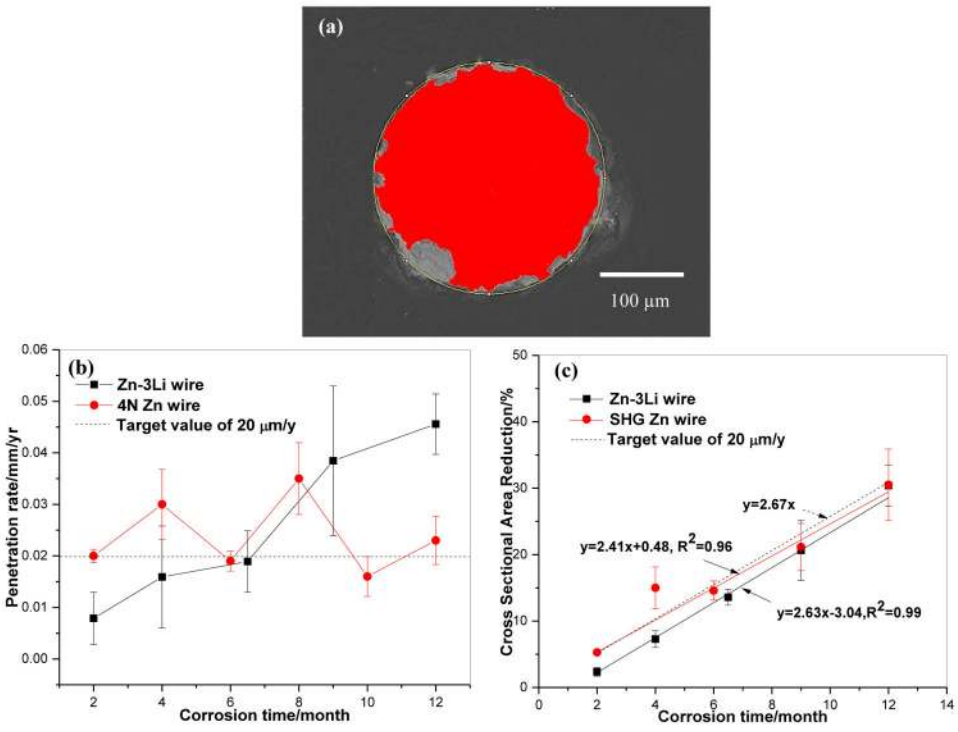

Fig 5.

(a) Typical ImageJ screenshot used for cross sectional analysis. The original local cross-sectional area (yellow) is approximated by an ellipse. The red area selected by thresholding is to represent the remaining Zn-3Li alloy. (b) Penetration rates calculated from reduction of cross sectional areas. (c) Cross sectional area reduction of alloy wires after explanation.

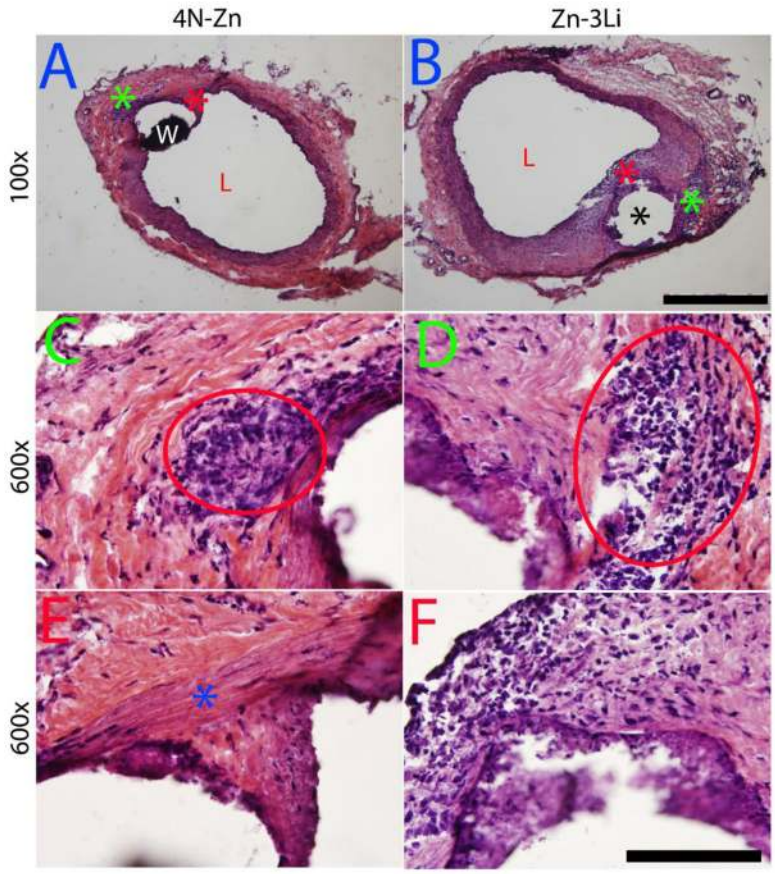

Fig 6.

Arterial explants stained with H&E at 11 months. Low magnification images show two subsequent areas selected for high magnification. “L” is the luminal opening of the artery. Scale bars are 500 μm and 100 μm for 100x and 600x, respectively.

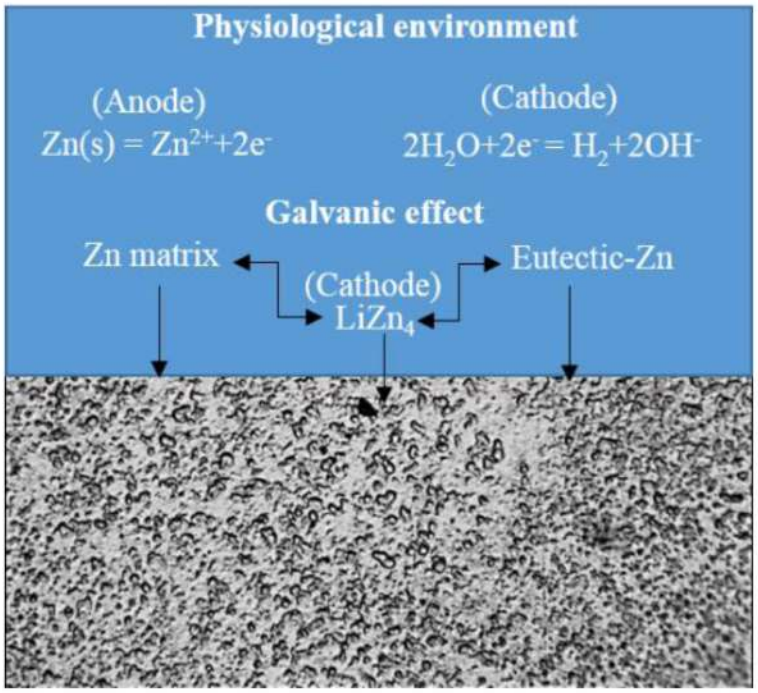

Fig 7.

Illustration of the galvanic effect between the Zn matrix and secondary phase in physiological environment

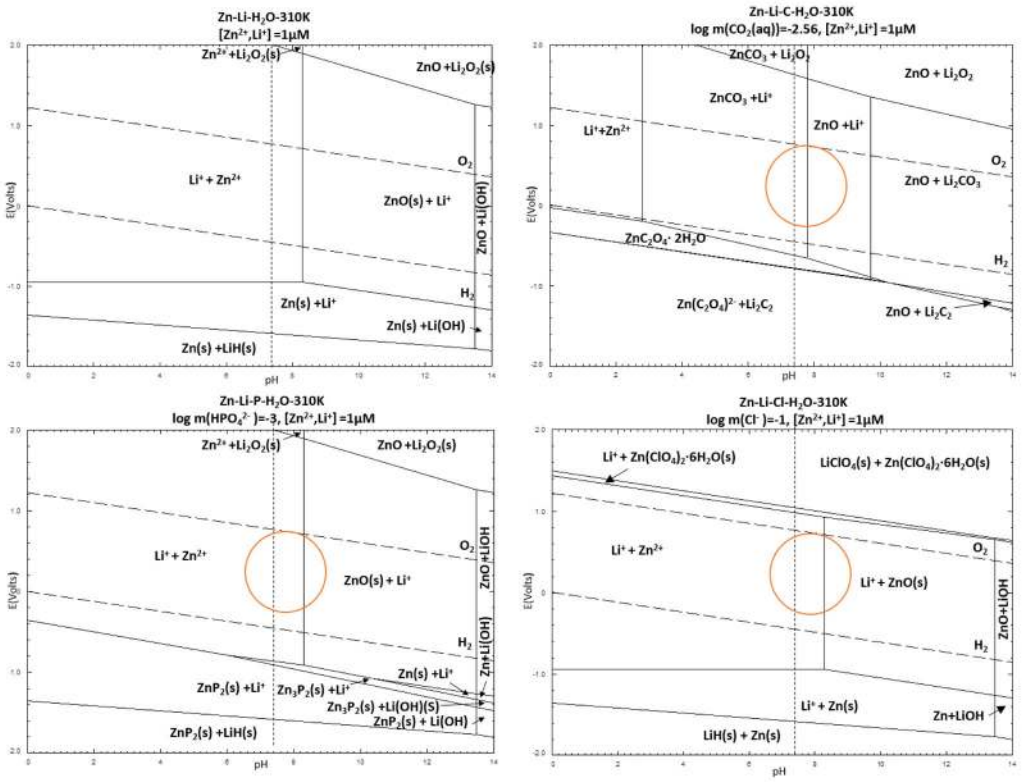

Fig 8.

Zn-Li-H_2O and Zn-Li-H_2O-X Pourbaix diagrams for physiological concentrations of X = {C, Cl, P } at 37°C. Physiological pH of 7.4 is shown by the dotted lines and physiological potential for tissue fluid is marked by the circles

Table 1

ICP-OES compositional analysis of Zn-3Li wires (at.%)

Sample	Li	Cu	Mg	Fe	Pb	Cd	Al	Ni	Zn
4N Zn	<0.01	<0.01	<0.01	<0.01	<0.01	<0.01	<0.01	<0.01	Bal.
Zn-3 Li	3.00	0.03	0.02	0.02	0.01	<0.01	<0.01	<0.01	Bal.

Table 2

Mechanical properties of 4N Zn and Zn-3Li wires

Sample	Yield strength (MPa)	Tensile strength (MPa)	Ductility %elongation	Ductility %area reduction	Hardness (Vickers)
4N Zn	86 ± 14	116 ± 13	50 ± 5	97 ± 2	42 ± 3
Zn-3Li	238 ± 60	274 ± 61	17 ± 7	74 ± 5	97 ± 2